ACSNANO
www.acsnano.org
ARTICLE

Atomistic Insights into the Oriented Attachment of Tunnel-Based Oxide Nanostructures

Yifei Yuan,[†,‡] Stephen M. Wood,[§] Kun He,[∥,†] Wentao Yao,[⊥] David Tompsett,[§] Jun Lu,[*,‡] Anmin Nie,[*,⊥] M. Saiful Islam,[*,§] and Reza Shahbazian-Yassar[*,⊥,#]

[†]Department of Materials Science and Engineering, Michigan Technological University, 1400 Townsend Drive, Houghton, Michigan 49931, United States

[‡]Chemical Science and Engineering Division, Argonne National Laboratory, 9700 South Cass Avenue, Argonne, Illinois 60439, United States

[§]Department of Chemistry, University of Bath, Bath BA2 7AY, United Kingdom

[∥]Department of Materials Science and Engineering, Shandong University, 17923 Jingshi Road, Jinan 250061, China

[⊥]Department of Mechanical Engineering, Michigan Technological University, 1400 Townsend Drive, Houghton, Michigan 49931, United States

[#]Department of Mechanical and Industrial Engineering, University of Illinois at Chicago, Chicago, Illinois 60607, United States

Supporting Information

ABSTRACT: **Controlled synthesis of nanomaterials is one of the grand challenges facing materials scientists. In particular, how tunnel-based nanomaterials aggregate during synthesis while maintaining their well-aligned tunneled structure is not fully understood. Here, we describe the atomistic mechanism of oriented attachment (OA) during solution synthesis of tunneled α-MnO_2 nanowires based on a combination of *in situ* liquid cell transmission electron microscopy (TEM), aberration-corrected scanning TEM with subangstrom spatial resolution, and first-principles calculations. It is found that primary tunnels (1 × 1 and 2 × 2) attach along their common {110} lateral surfaces to form interfaces corresponding to 2 × 3 tunnels that facilitate their short-range ordering. The OA growth of α-MnO_2 nanowires is driven by the stability gained from elimination of {110} surfaces and saturation of Mn atoms at {110}-edges. During this process, extra [MnO_x] radicals in solution link the two adjacent {110} surfaces and bond with the unsaturated Mn atoms from both surface edges to produce stable nanowire interfaces. Our results provide insights into the controlled synthesis and design of nanomaterials in which tunneled structures can be tailored for use in catalysis, ion exchange, and energy storage applications.**

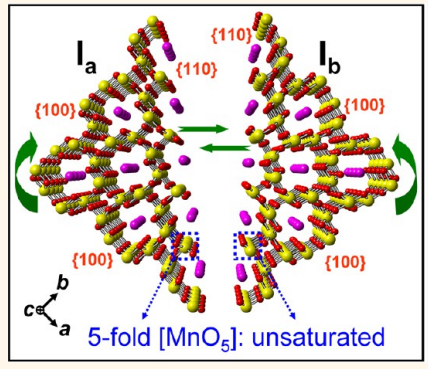

KEYWORDS: *nanowire, oriented attachment, tunnel, interface, surface structure*

Considerable attention has been devoted to the study of inorganic compounds with open tunnel structures. Materials in this category include, but are not limited to, zeolites,[1,2] titanium silicates,[3] TiO_2[4,5] and MnO_2-based molecular sieves.[6−10] The characteristic tunnel-based structure allows these materials to accommodate and transport charge carriers (also called tunnel stabilizers) with different sizes and charges, enabling their wide application in catalysis, ion exchange and energy storage.[11−14] Controlled synthesis is necessary to produce tunnel-based nanostructures with various tunnel sizes, morphologies and atomic ordering. However, this process is not fully understood and requires fundamental understanding of the growth mechanisms on the nanoscale and even at the single-tunnel level.

Solution-based synthesis is often used to prepare tunnel-based materials, in the form of one-dimensional nanostructures.[15−23] The growth mechanism is generally believed to be an oriented attachment (OA) process where primary particles aggregate by sharing a common planar interface and form a secondary particle with a uniform orientation, allowing the rational design of hierarchical nanostructures for functional

Received: September 2, 2015
Accepted: December 9, 2015
Published: December 9, 2015

DOI: 10.1021/acsnano.5b05535
ACS Nano 2016, 10, 539−548

devices.[19,24−26] The driving force for the growth is thought to be the reduction of the surface energy when primary particles attach together.[27−29] The as-formed OA interface is usually imperfect,[30,31] because of the complex nature of different tunnel−tunnel intergrowths[32,33] as well as the strong interaction between tunnels and the inner stabilizers.[34,35] It is still unclear how primary tunnels grow to form secondary nanowires with precise alignment of tunnels. Understanding the atomic structure of tunnel-based materials during growth is crucial for designing nanomaterials in which the tunneled structure can be tailored and controlled for desired applications.

α-MnO_2 represents an important family of tunnel-based structures with well-aligned 2 × 2 (4.6 × 4.6 Å^2) and 1 × 1 (1.9 × 1.9 Å^2) tunnels.[16] Polyhedral and atomic models of α-MnO_2 are illustrated in Figure 1. The larger 2 × 2 tunnels are generally

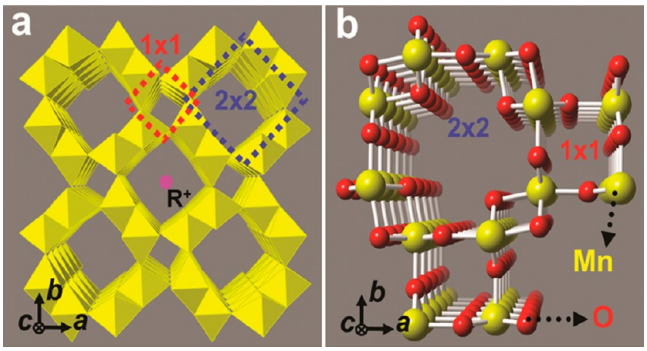

Figure 1. Crystal structures of α-MnO_2. (a) [MnO_6] octahedra model; (b) atomic model viewed along [001] (*c*-axis). The 2 × 2 and 1 × 1 tunnels are indicated by blue and red dashed squares, respectively, in (a). The typical definition of a tunnel is based on the number of [MnO_6] octahedra in each tunnel wall. R^+ indicates the position of 2 × 2 tunnel stabilizers such as NH_4^+, Ba^{2+}, and K^+.

stabilized by various cations, such as NH_4^+, Ba^{2+}, and K^+.[19] Here, K^+-stabilized α-MnO_2 nanowires were investigated to understand their tunnel-based structures during growth. For the first time, the morphology evolution of α-MnO_2 nanowires in an aqueous solution environment was dynamically observed using liquid cell transmission electron microscopy (TEM), and subangstrom imaging of the tunneled interfaces was obtained using aberration-corrected scanning TEM (AC-STEM). The structural characterization was complemented by *ab initio* calculations to elucidate the surface energetics of K^+-stabilized α-MnO_2. It was found that primary α-MnO_2 nanowires prefer to attach together laterally along their {110} surfaces to form larger secondary nanowires facilitated by the reduction of their surface energy. In contrast to the conventional 1 × 1 and 2 × 2 tunnels, the {110} interfaces are composed of 2 × 3 tunnels parallel to the 1 × 1 and 2 × 2 tunnels. The formation of the 2 × 3 tunnel-based {110} interfaces during the growth process is driven by reduction of the surface energy and bonding of [MnO_5] units exposed at {110} surfaces with [MnO_x] radicals in solution. The importance of K^+ in forming the 2 × 3 tunnel-based interfaces during the oriented attachment growth is also demonstrated.

RESULTS AND DISCUSSION

Morphology and Phase Evolution. The morphology and phase evolution of MnO_2 nanowires under different reaction times were studied using X-ray diffraction (XRD) and transmission electron microscopy (TEM), and the results are presented in Figure 2. XRD results show that the characteristic peaks (red indices) of α-MnO_2 appear when the reaction time reaches 1.5 h. When the reaction time was increased from 1.5 to 9 h, the size and crystallinity of nanowires gradually improved, as indicated by the peak sharpening and intensity enhancing, respectively. From 9 to 12 h, the XRD peaks do not show any obvious difference, indicating stable and well-formed α-MnO_2. Layered δ-MnO_2, although not detected by XRD (probably on account of its low concentration and partial peak overlapping), was found by TEM to coexist with α-MnO_2 nanowires grown for less than 1.5 h. However, for longer reaction times, no evidence of δ-MnO_2 was found. This finding agrees well with previous reports stating that layered δ-MnO_2 functions as the precursor for tunnel-based α-MnO_2 nucleation and growth.[18] Figure 2 also shows that the primary α-MnO_2 nanowires gradually attached to each other and formed secondary α-MnO_2 nanowires with a larger diameter (marked as red dotted circles). This is indicative of a lateral OA mechanism operating during the growth of α-MnO_2.

The growth rate greatly decreased after 9 h, as confirmed by a slight change in the diameter of nanowires produced for reaction times between 9 and 12 h. The thickness contrast in each secondary nanowire is relatively uniform along the nanowire length. However, this is not the case radially. This indicates that primary nanowires share a common growth direction. The energy dispersive spectrometer (EDS) results in Figure 2f confirm the existence of a small concentration of potassium (K^+), consistent with use of a K^+-containing solution.

To confirm that the secondary nanowires are formed by the ordered alignment of several primary nanowires, we investigated secondary nanowires using *in situ* liquid cell TEM.[27,36−38] Interestingly, a high dose electron beam was sufficient to trigger the dissolution of secondary α-MnO_2 nanowires immersed in KCl solution and break them down to the original building blocks. The corresponding movie illustrating this process is provided as Movie S1 (played in real time) in the Supporting Information, and Figure 3 shows *in situ* time-lapse TEM images of the morphology evolution of a secondary α-MnO_2 nanowire during this dissolution process. From 0 to 16 s, the secondary nanowire experienced isotropic dissolution both radially and axially in KCl solution. It is notable that the interface region (green arrows) was gradually etched during the dissolution process, which is demonstrated by the increase in brighter contrast. This finding indicates that the OA interface is metastable during the solution-based synthesis process. After 20 s, the interface was completely eliminated causing the detachment and misorientation of the two primary α-MnO_2 nanowires (the rotation directions are marked by the yellow arrows in Figure 3f−h). To confirm that the electron beam is the driving force for the dissolution, we intentionally kept the secondary nanowire in the liquid environment for 1 h before it was exposed to the electron beam for the *in situ* recording. Then, the beam was turned on and the secondary nanowire was found in the well grown morphology with the OA interface clearly seen, indicating that no dissolution occurred when there was no electron beam. Hence, the dissolution of the oriented attachment interface can be attributed to the use of the electron beam.

We propose that the radiation chemistry plays a critical role in the dissolution and detachment of α-MnO_2 nanowires inside the TEM liquid cell. It has been reported that a water-based solution, when subjected to a high dose electron beam, decomposes into excited and ionized species such as H^+, OH^-,

DOI: 10.1021/acsnano.5b05535
ACS Nano 2016, 10, 539−548

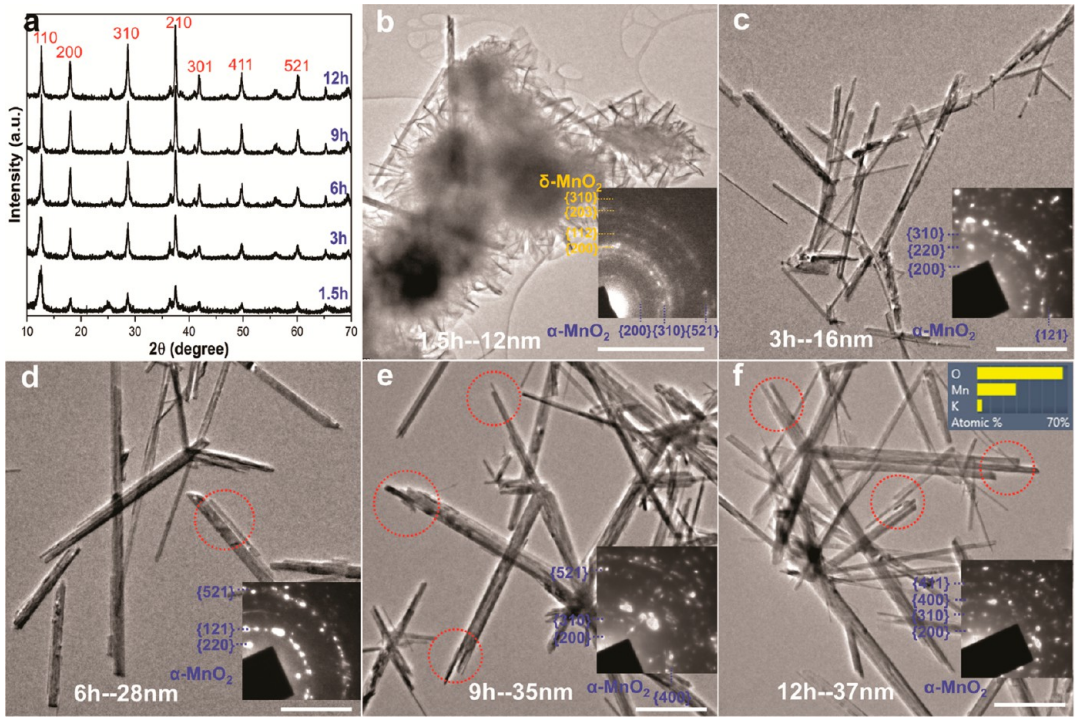

Figure 2. (a) XRD patterns for hydrothermally prepared α-MnO_2 nanowires for reaction times of 1.5, 3, 6, 9, and 12 h; (b–f) TEM images and selected area electron diffraction patterns (insets) of the samples after different reaction times. The upper inset in (f) shows the EDS results confirming the presence of K^+. Scale bars are 100 nm.

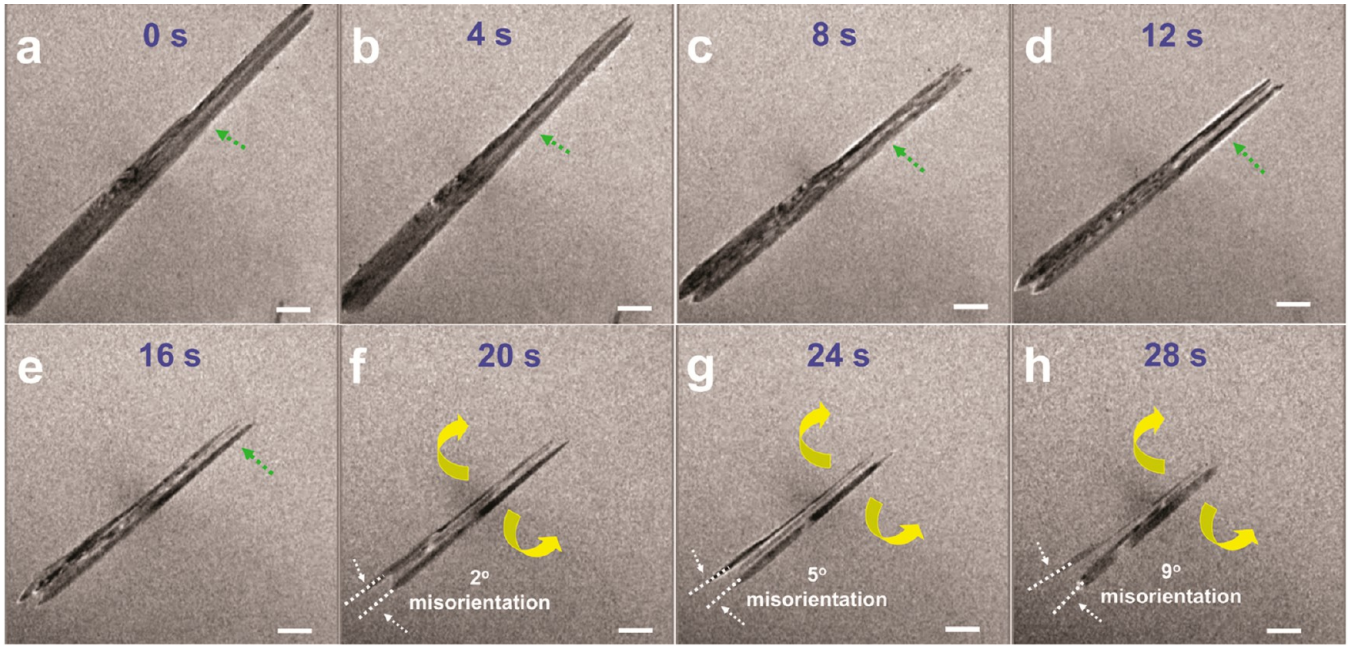

Figure 3. *In situ* time-lapse TEM images show the morphology evolution of a secondary α-MnO_2 nanowire in the liquid cell during its dissolution process driven by the incident electron beam. The green arrows in (a–e) indicate the OA interface region between two primary α-MnO_2 nanowires experiencing gradual dissolution, and the yellow curved arrows in (f–h) indicate the rotation direction (detachment) between the two primary nanowires. Scale bars in all: 150 nm.

H_2, and H_2O_2.[39] Due to the different reaction kinetics among these species, for an initially neutralized solution, the entire liquid cell will gradually exhibit an increased H^+ concentration and reduced pH.[40] The acid environment, according to *ex situ* solution synthesis experiments for α-MnO_2 nanostructures, is detrimental to the maintenance of larger tunnels such as 2 × 2 and 2 × 3 tunnels because the stabilizing effect of larger cations is weakened by H^+ in solution.[34] In the case of our KCl solution (with initial pH = 7) that contains secondary α-MnO_2 nanowires, the solution environment would gradually become H^+ rich under exposure to an electron beam. Such an acidic environment destabilizes the K^+ residing inside the 2 × 2

DOI: 10.1021/acsnano.5b05535
ACS Nano 2016, 10, 539–548

tunnels and facilitates the ion exchange process between K^+ and H^+. Due to the much weaker tunnel stabilizing effect of H^+ compared to K^+,[41] the 2 × 2 tunnel-based structure will not be stable any more resulting in its gradual dissolution. The interface region is therefore more vulnerable under electron beam radiation and the removal of K^+ stabilizers. This dynamic observation of the breakdown process directly confirms the existence of interfacial attachment that controls the growth process of α-MnO_2 nanostructures in solution environment.

Atomic Structure of the OA-Induced Interface. Figure 4a shows a TEM image of one secondary α-MnO_2 nanowire

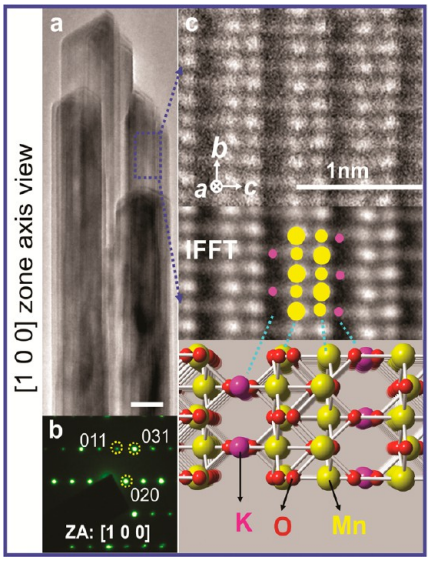

Figure 4. (a) A TEM image of secondary α-MnO_2 nanowires taken along [100]; (b) SAED pattern of the same region as (a); (c) a HAADF image of the blue-framed region of a primary nanowire in (a). The corresponding IFFT is given in the middle with the atomic model illustrated at the bottom, where yellow dots represent Mn, red O, and pink K^+. The signal of K^+ during HAADF imaging is weaker than that of Mn due to its smaller atomic weight. Scale bar in (a) is 10 nm.

viewed down [100]. The nanowire is composed of several well-aligned primary nanowires with diameters ranging from 10 to 20 nm. Despite the aggregation of multiple primary nanowires, the secondary nanowire still appears to be monocrystalline, as confirmed by the corresponding selected area diffraction patterns (SAED), shown in Figure 4b. A high angular annular dark field (HAADF) image of one primary unit is shown in Figure 4c with the corresponding inverse fast Fourier transform (IFFT) given in the middle and the atomic model at the bottom. The 2 × 2 tunnel can be clearly seen to be surrounded by [MnO_6] octahedral units (yellow dots) and supported by K^+ atoms (pink dots) in their center, which agrees well with the atomic structure model. Results of the elemental analysis and the confirmation of the tunnel alignment along [001] are shown in Figure 6. On the basis of the SAED and HAADF results, the growth direction of α-MnO_2 nanowires is determined to be [001], which is parallel to the tunnel direction. Imaging down [100] did not reveal clearly any interfaces between primary nanowires, implying that this direction is not parallel to the OA interface.

Figure 5a is the [1 $\bar{1}$ 1] view of another secondary nanowire, which exhibits monocrystalline characteristics, as indicated by the SAED pattern in Figure 5b. The fact that secondary α-

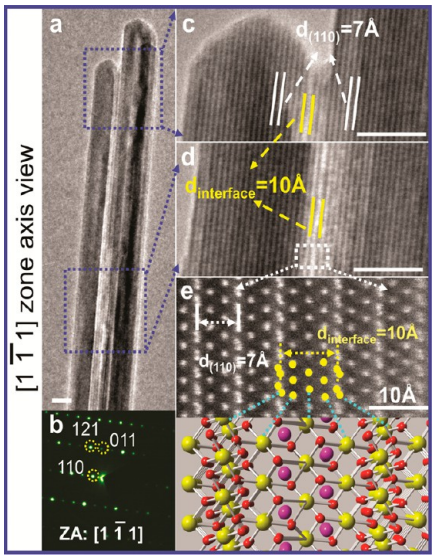

Figure 5. (a) A TEM image of one secondary α-MnO_2 nanowire taken along [1 $\bar{1}$ 1], where the {110} interface can be directly imaged; (b) SAED pattern of the same nanowire in (a); (c and d) HRTEM images of the OA-induced interface from the terminated and center parts of the nanowire, respectively; (e) a HAADF image of the white-framed interface region in (d). The corresponding atomic model is illustrated at the bottom, where yellow dots represent Mn, red O, and pink K^+. Scale bars in (a, c, and d) are 10 nm.

MnO_2 nanowires do not show multiple diffraction spots implies that the primary nanowires are precisely oriented with respect to each other. The interface is parallel to the electron beam when viewed down [1 $\bar{1}$ 1], and it clearly extends throughout the entire secondary nanowire. HRTEM images of the interface at different locations (marked by the blue dotted squares) are given in Figure 5c,d. Within each individual primary nanowire, the $d_{\{110\}}$ spacing is 7 Å, while this value increases to 10 Å for the interfacial planes ($d_{interface}$). The HAADF imaging of the interface along [1 $\bar{1}$ 1] is given in Figure 5e with the corresponding atomic model shown at the bottom. According to this atomic image, the {110} alignment of the interfaces is associated with the ordering of Mn atomic columns. The larger $d_{interface}$ (10 Å) is a result of the addition of an extra row of Mn atoms in the center, which is probably introduced during the lateral OA growth. This result indicates that the α-MnO_2 {110} surface can act as the common surface across which the primary nanowires attach to each other. The finding that the {110} interface spacing is larger than that of α-MnO_2 {110} spacing also suggests that the growth of α-MnO_2 in solution is an "imperfect" OA process, as defined in other materials systems.[42]

To efficiently explore the atomic arrangement of the OA interface, a secondary nanowire was examined parallel to the nanowire axis (Figure 6). The [001] ABF image in Figure 6a shows that the nanowire has a square-shaped cross section with four {100} lateral surfaces. The red dashed lines in Figure 6a also indicate several {110} dark stripes inside the nanowire, indicating heterogeneity in the structure. Close examination of several other cross-sectioned specimens perpendicular to the nanowire axis indicates that most lateral surfaces of the nanowires correspond to {100} planes, and that the {110} stripes are always present (Supporting Information Figure S1).

The bright central area in Figure 6a indicates that the secondary nanowire has a hollow section in the middle. Figure

DOI: 10.1021/acsnano.5b05535
ACS Nano 2016, 10, 539–548

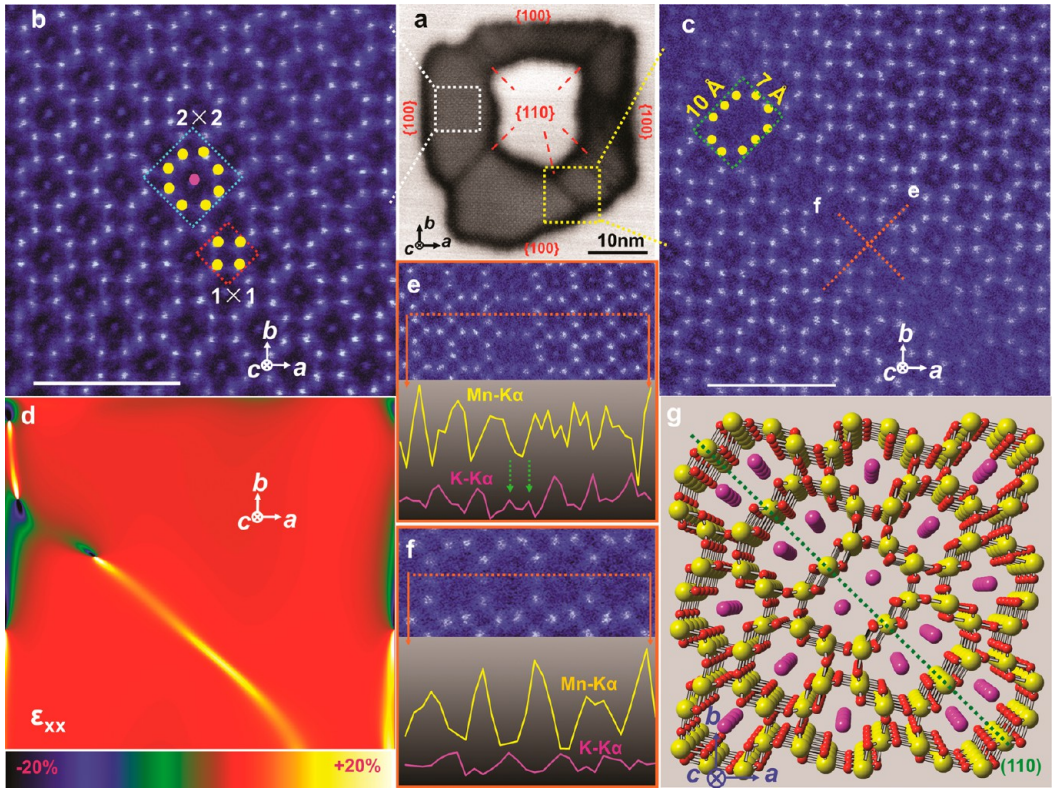

Figure 6. (a) An ABF image of an α-MnO_2 nanowire cross section viewed along the [001] zone axis. White and yellow squares indicate a perfect crystalline area and {110} defect-rich stripes, respectively. (b) False-colored HAADF image of the perfect crystalline area. Blue and red squares indicate typical 2 × 2 and 1 × 1 tunnels of α-MnO_2, respectively, and yellow and pink dots indicate atomic columns of Mn and K^+, respectively. (c) False-colored HAADF image of the {110} defect-rich stripe revealing the 2 × 3 tunnels; (d) ε_{xx} mapping near the 2 × 3 tunneled {110} interface; (e and f) EDS line scans across a 2 × 3 tunnel-based interface along the two vertical directions labeled "e" and "f" in (c); (g) the atomistic model illustrating the {110} interface structure, with yellow balls for Mn, red for O and pink for K^+. Scale bars in (b and c) are 2 nm.

6b is a HAADF image of the well-crystallized area where typical 1 × 1 and 2 × 2 tunnels of α-MnO_2 are clearly observed. Closer inspection reveals that 1 × 1 tunnels are empty while each 2 × 2 tunnel is occupied by a column of atoms in its center. These atoms were later confirmed to be K^+ (Figure 6e). The position of K^+ in the 2 × 2 tunnels was determined to be the Wyckoff 2a site (0, 0, 0) and the nanowire composition to be α-$K_{0.25}MnO_2$.

To assist in determining the atomic-scale structure, we also performed *ab initio* density functional theory (DFT) calculations on the α-$K_{0.25}MnO_2$ bulk system with K^+ ions on either the Wyckoff 2a (0, 0, 0) or 2b (0, 0, 1/2) sites, as illustrated in Figure S2. From these simulations, the 2a site was found to be at least 300 meV lower in energy than the 2b site. This difference is significantly greater than the thermal energy at room temperature ($k_BT \sim 26$ meV), which suggests that the predicted position of K^+ ions in the central 2a site is in good agreement with the experimental observation.

The atomic-resolution HAADF image in Figure 6c obtained from one striped area shows that this stripe actually consists of 2 × 3 tunnels that are aligned parallel to the characteristic 1 × 1 and 2 × 2 tunnels of α-MnO_2. The width of 2 × 3 tunnels was measured to be 10 Å, which is consistent with the $d_{interface}$ spacing at the {110} interface obtained from Figure 5c. This observation reveals that the 2 × 3 tunnel-based stripe is in fact the {110} interface *via* which primary α-MnO_2 nanowires laterally attach to each other. Figure 6d shows the ε_{xx} map around the {110} stripe, where a larger amount of strain is evident at the interface.

Atomic-resolution elemental analysis around 2 × 3 tunnels was performed by taking EDS line scans along two vertical directions marked "e" and "f" in Figure 6c; the results are plotted in panels e and f of Figures 6, respectively. The linear profile of Mn and K along direction e indicates that Mn is present in the 2 × 2 tunnel walls, with one K signal peak detected at the center of each 2 × 2 tunnel, and two K signal peaks (green arrows in Figure 6e) inside the 2 × 3 tunnel. The linear profile around the 2 × 3 tunnels along direction f reveals that the tunnel walls are still constructed from Mn, with one K signal peak detected at the tunnel center. On the basis of these results, the atomic configuration around a {110} interface region was constructed and shown in Figure 6g. The tunnel walls for both 2 × 2 and 2 × 3 tunnels are built from Mn atoms. Compared to the normal 2 × 2 tunnels stabilized by only one K^+ atom column, two K^+ columns exist inside the 2 × 3 tunnels. The presence of the extra K^+ column is found to stabilize the 2 × 3 tunnel-based OA interface of α-MnO_2, prevent structural collapse, and thus maintain the good crystallinity of solution-grown α-MnO_2 nanowires. This significant finding is in agreement with the conjecture that larger tunnels require more cation columns as tunnel stabilizers,[43] and implies the important role of excess cations in solution during OA growth of tunneled structures.

The fact that tunnel-based interfaces are always parallel to {110} planes indicates that the solution-based OA growth of α-MnO_2 is a surface-controlled process. To examine this issue further, the energetics of a range of surfaces of α-MnO_2 in the

DOI: 10.1021/acsnano.5b05535
ACS Nano 2016, 10, 539–548

presence of K^+ were explored by using well-established DFT methodology.[44−46] The wide range of surface planes were initially selected based on the low energy surfaces found from previous studies of pure α-MnO_2.[44] In Table 1, we list the calculated surface energies for α-$K_{0.25}MnO_2$. Such an analysis shows that the lowest energies correspond to the (100) and (110) surfaces. Compared to other surfaces, the (211) surface also exhibits low energy, which was, however, not observed experimentally. Even if the (211) OA interface exists, the lateral surfaces of one secondary nanowire and its atomic arrangement along [001] would both be disrupted. The TEM observation indicates that the lateral surfaces of the nanowires are smooth and the atomic columns along [001] are well ordered (each column is clearly distinguishable with good contrast in the HAADF images in Figures 6 and 7). These two facts indicate the low chances of (211) interface formation, which is thus not further explored in this work. Nevertheless, the DFT results clearly show that the (100) surface is considerably lower in energy than all other terminations, which is confirmed experimentally by Figure 6a (and Figure S1) showing the four lateral surfaces of α-MnO_2 nanowires to be parallel to {100} planes. The (110) surface is sufficiently favorable that we would expect it to dominate the morphology of the nanoparticles during the initial growth stages, in agreement with the experimental finding that interfaces are formed parallel to {110} planes.

Table 1. Calculated (DFT + U) Surface Energies for $K_{0.25}MnO_2$

Miller index	surface energy (Jm^{2-})
(100)	0.44
(110)	0.74
(211)	0.78
(210)	1.14
(001)	1.17
(101)	1.17
(201)	1.19
(111)	1.35

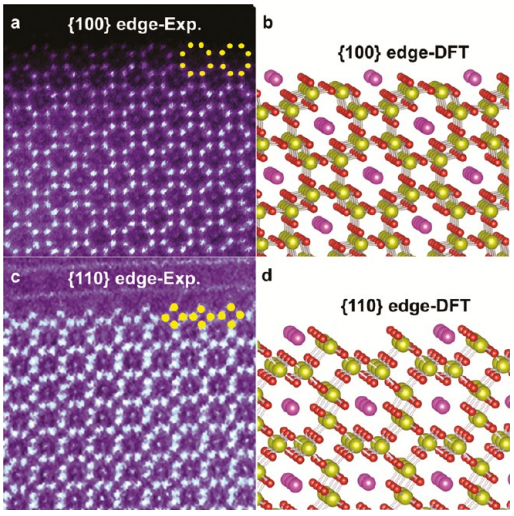

Figure 7. (a) Atomic-resolution HAADF image of a (100) edge in an α-$K_{0.25}MnO_2$ nanowire compared with (b) the calculated relaxed (100) surface structure of α-$K_{0.25}MnO_2$. (c) Atomic-resolution HAADF image of a (110) edge in an α-$K_{0.25}MnO_2$ nanowire compared with (d) the calculated relaxed (110) surface structure of α-$K_{0.25}MnO_2$. Yellow balls are Mn, red are O, and pink are K.

Atomistic Mechanism for Formation of 2 × 3 Tunnel-Based {110} Interfaces. We now turn to the edge structure of the low energy surfaces {100} and {110}, in an attempt to understand how the fundamental characteristics of the exposed surfaces in solution drive the formation of 2 × 3 tunnel-based {110} interfaces. The structure of a (100) surface obtained from HAADF imaging is shown in Figure 7a, with the atomistic relaxed surface from DFT calculations given for comparison in Figure 7b. The (100) surface is essentially composed of a series of intact 2 × 2 tunnels with a bisected 2 × 2 tunnel sitting between the intact tunnels, agreeing well with the simulated structure. There is little calculated distortion between the unrelaxed and relaxed surface for this cleavage plane, as is typical for energetically favorable surfaces. In addition, Figure 7b shows that the Mn ions in the surface region remain well coordinated with 75% remaining in 6-fold coordination, identical to Mn ions in the bulk. The remaining 25% of Mn ions have 5-fold coordination and are unsaturated. Moreover, half of the surface K^+ ions reside within intact 2 × 2 tunnels in their preferred 8-fold coordination (as found in the bulk structure), with the other half maintaining a reduced 4-fold coordination. These structural features are likely to account for the low surface energies calculated for the {100} surfaces, and indicate that such {100} surfaces will be stable during the OA process.

The fact that the {100} surface is covered by 2 × 2 tunnels instead of 1 × 1 tunnels is important for the improvement in performance of α-MnO_2 nanostructured materials. The direct exposure of large 2 × 2 tunnels is likely to reduce the distance and energy barrier for ion diffusion, improving the rate performance of α-MnO_2 in applications such as rechargeable battery electrodes,[47−50] supercapacitors[51−53] and Li−O_2 battery catalysts.[54−57] Indeed, future generations of these energy storage technologies will depend crucially on new nanostructured materials.

The structure of a (110) surface before the OA process begins can be seen in the HAADF image in Figure 7c. The simulated atomistic structure of the same surface is given in Figure 7d. The (110) surface forms a step-like edge that is covered by 1 × 1 tunnels, matching the theoretical model very well. Like the (100) surface, there is relatively little calculated distortion between the unrelaxed and simulated relaxed structures, indicating that this surface is relatively stable. The atomistic model also shows that the Mn ions at the (110) surface remain in a high coordination environment, with two-thirds in 6-fold coordination sites. The remaining Mn ions, corresponding to the most exposed ions, are in 5-fold coordination. Furthermore, the outermost K^+ ions are stabilized by a slight relaxation into the surface, which has the effect of increasing their coordination number from 4 to 5. The (110) surface has more unsaturated [MnO_5] units than the (100) surface, a consequence of which is that the (110) surface is predicted to be less stable than (100). All the other surfaces have larger amounts of unsaturated [MnO_5] units, with some even containing [MnO_x] ($x < 5$) units, making them unstable in solution.

On the basis of the subangstrom resolution image of the (110) edge structure in Figure 7, we propose an atomistic model to explain the formation of 2 × 3 tunnels at a {110} interface between two primary crystals (termed I_a and I_b). This

DOI: 10.1021/acsnano.5b05535
ACS Nano 2016, 10, 539−548

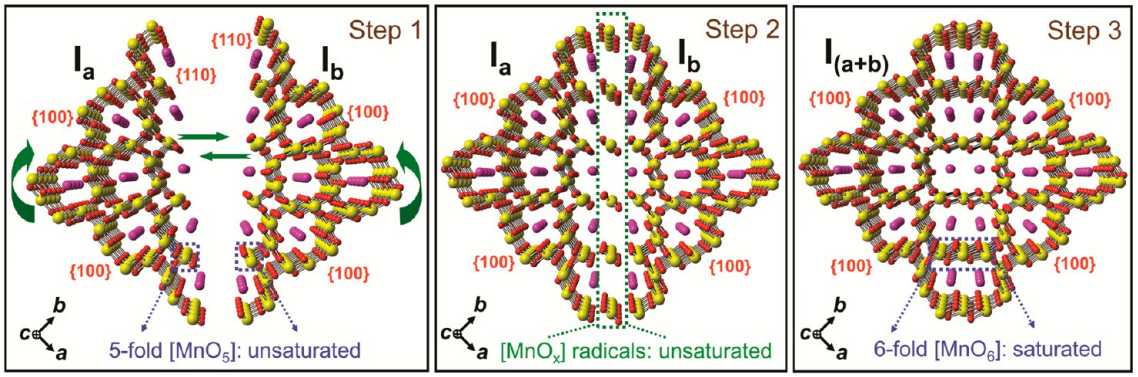

Figure 8. Schematic diagrams illustrating the formation of a 2 × 3 tunnel-based {110} interface during OA of two primary α-MnO_2 nanowires at the atomic level. The nanowires (I_a and I_b) are orientated parallel to the *c* axis ([001]) with their stable {100} surfaces and metastable {110} surfaces exposed in solution. The curved and straight green arrows in Step 1 indicate the rotating and linear approaching movements of the primary nanowires, respectively. Surrounding the nanowires is the aqueous solution environment containing $MnSO_4$ and $KMnO_4$ in excess.

process is illustrated in Figure 8 with perspective views, and is divided into three steps. At the beginning of the first step when I_a and I_b initially form in solution with random but close orientations, the dominant surfaces should be {100} and {110} as both types of surface possess lower surface energies than other crystal planes. Since {110} surfaces are less stable than {100}, there is a tendency among the primary crystals to attach to each other along their {110} surfaces to minimize the overall energy. Consequently, I_a and I_b approach each other through van der Waals forces, which has been widely reported for the OA growth of nanostructures,[27,28,58] and orient themselves parallel to their common {110} surfaces.

In the second step, as I_a and I_b come into close proximity, the large repulsive force between exposed K ions on the {110} surfaces prevent them bonding. However, extra [MnO_x] radicals in the surrounding solution are able to squeeze between the I_a and I_b crystals.

In the third step, the extra [MnO_x] radicals between the crystals bond with the dangling [MnO_5] units from both {110} surfaces, resulting in the elimination of the two surfaces and formation of one 2 × 3 tunnel-based {110} interface. This process should be energetically favorable as the unsaturated [MnO_5] units of the {110} surfaces become saturated, forming the more stable [MnO_6] units. Following similar steps, more primary α-MnO_2 nanowires can be gradually attached together across their exposed {110}, and the diameter of the secondary nanowire could be gradually increased during the subsequent high order attachment in solution.

The lateral OA mechanism results in the aggregation of only a few primary nanowires instead of long-range ordered structures. This should be due to the gradual decrease of the OA driving force, namely the elimination of pairs of {110} surfaces. At the early stages when a substantial number of {110} surfaces exist in the solution, the lateral OA *via* {110} should occur in a large scale to eliminate the overall surface energy of the system by elimination of {110} surfaces. At later stages when a limited number of {110} surfaces remain and the secondary nanowires are well grown, the OA growth of α-MnO_2 nanowires is thus terminated. The effect of K^+ during the solution growth of α-MnO_2 nanostructures has been widely studied.[34,59−61] However, these reports have focused on the formation of α-MnO_2 phase instead of the defective interface. The conclusion has been that α-MnO_2 can only nucleate and grow when there are excess K^+ in solution because the large 2 × 2 tunnels need to be stabilized by certain cations such as K^+. Otherwise, other MnO_2 polymorphs (β-MnO_2 or γ-MnO_2) with smaller 1 × 1 and 1 × 2 tunnels will form when there are few or no K^+. On the basis of our work, we find that K^+ ions are important in the formation of the {110} OA interface because two K^+ atomic columns are present in one large 2 × 3 tunnel. It is reasonable to expect that the {110} interface, which is composed of even larger 2 × 3 tunnels, would not exist if there are no more K^+ in the solution during the lateral OA stage to support the large tunnels. The presence of [MnO_x] radicals in aqueous solution and the exact Mn oxidation state ("*x*" value) are difficult to be verified in the current experiment due to the strong effect from the liquid environment as well as various types of structural Mn−O bonds. Nevertheless, there might be other methods to confirm [MnO_x], such as *in situ* X-ray Absorption Spectroscopy (XAS) providing electronic structure information. Such an experiment requires a sealed liquid cell with an X-ray transparent window, X-ray with high penetration energy, and also proper data interpretation to get rid of the signals from other Mn−O bonds; this is clearly a topic for future work.

Although this study is not exhaustive, it does highlight an important area for further work on tunnel-based oxide nanostructures. Indeed, future studies could include rational design of various tunneled structures with ideal hierarchy, controllable dimension and morphology, and large-scale molecular dynamics simulations in solution-based systems.

CONCLUSION

K^+-stabilized α-MnO_2 nanowires were hydrothermally synthesized by an orientated attachment (OA) growth mechanism, and the structures of the nanowires and their interfaces were explored at the atomic scale.

First, it was determined that primary α-MnO_2 nanowires prefer to combine laterally with each other by sharing their {110} surfaces to construct secondary α-MnO_2 nanowires. This OA process is driven by the reduction of the surface energy and the tendency of dangling [MnO_5] units at {110} surfaces to be saturated to form [MnO_6] by bonding with [MnO_x] radicals in solution.

Second, the resulting {110} interfaces are defective and composed of 2 × 3 tunnels supported by two K^+ columns rather than a normal 2 × 2 tunnel supported by one K^+ column. The presence of K^+ excess in solution plays an important role during the formation and stabilization of the OA interface.

DOI: 10.1021/acsnano.5b05535
ACS Nano 2016, 10, 539−548

This work provides greater fundamental understanding of the atomic structure at the surface and OA interface in one-dimensional tunneled α-MnO_2. A key example is the finding that the (100) surface is covered by 2 × 2 tunnels while (110) is covered by 1 × 1 tunnels; this suggests faster reaction at (100) surfaces than that at (110), since most reactions occur inside the large 2 × 2 tunnels. This understanding could guide selective surface engineering to synthesize α-MnO_2 nanostructures for improved functional performance.

With the increasing interest in crystal facet engineering, the importance of surface chemistry demonstrated here could inspire related research on tunnel-based oxide nanostructures for potential applications in catalysis, sensors and energy storage.

METHODS

Sample Preparation. α-MnO_2 nanowires were produced by a hydrothermal process using $KMnO_4$ and $MnSO_4$ as the reactants.[22] The reaction was carried out in a Teflon-lined stainless steel autoclave at 160 °C for 1.5, 3, 6, 9, and 12 h to obtain α-MnO_2 nanowires at different stages of growth. To prepare electron-transparent slices of the nanowire cross sections, the nanowires were first mixed with cold mounting epoxy resin (EPOFIX, Electron Microscopy Sciences) under 10 min supersonic vibrations. Hardener (EPOFIX, Triethylenetetramine, Electron Microscopy Sciences) was then added into the solution to facilitate the solidification process in atmosphere at 60 °C for 24 h. After that, the solid solution was fixed on the sample stage of a Leica Ultracut UCT ultramicrotome equipped with a diamond knife. The nanowires were mechanically cut into slices at a feeding step size of 500 nm.

Sample Characterization. Phase analysis was performed using powdered X-ray diffraction (XRD). The representative diameter of each sample was obtained statistically by averaging the diameters of tens of nanowires from different sample areas under low-magnification TEM. The atomic structure was analyzed using a spherical aberration-corrected JEOL JEM-ARM200CF scanning transmission electron microscope (STEM) equipped with a 200 kV cold-field emission gun, annular bright field (ABF) and high angle annular dark field (HAADF) detectors, and an energy dispersive spectrometer (EDS). A 22-mrad-probe convergence angle was used for all STEM images. The HAADF images were captured using a 90-mrad inner-detector angle.

The *in situ* liquid cell TEM experiment was carried out using a commercialized liquid holder (Protochips. Poseidon 500) inside the JEOL JEM-ARM200CF STEM at an acceleration voltage of 200 kV. Two chips made of Si substrates with 50 nm thick Si_3N_4 layers were used to construct the liquid cell with the inner space of 150 nm, enabling good electron transparence. Since the Si_3N_4 was the working surface that directly contacted the aqueous solution, before assembling the liquid cell, the Si_3N_4 surfaces were washed with methanol and then plasma cleaned for 1 min to remove contaminants and make the surface hydrophilic. The size of each Si_3N_4 window (where Si substrate was etched beforehand) was 550 × 20 μm^2. The two windows were aligned in parallel so that the imaging area was maximized. The flow of liquid into the cell was using a coaxial PEEK tubing with an inner diameter of 100 μm and the tubing was connected with a syringe, which contained 0.5 mL KCl solution. The concentration of K^+ was kept at 0.03 mol/L, the same as it was in the actual solution during the hydrothermal synthesis. The electron dose rate was maintained approximately at 5.5 (±0.5) × 10^3 e/(nm^2·s).

***Ab Initio* Computer Modeling.** Surface calculations were performed using density functional theory (DFT) with PAW potentials, as implemented in the VASP code.[62] The generalized gradient approximation (GGA) of Perdew–Burke–Ernzerhof (PBE)[63] was applied with a Hubbard U correction, as this has been demonstrated to give a good description of the ion insertion, surface energies and electronic structure of α-MnO_2,[44,45] and other transition metal oxides.[64] A planewave basis set cutoff energy of 520 eV and a minimum grid of 3 × 3 × 7 k-points was used in the Brillouin zone for bulk calculations. The calculated lattice parameters for $K_{0.25}MnO_2$ agree well with experiment, as shown in Supporting Information Table S1, although the common tendency for PBE + U to slightly overestimate the unit cell volume is apparent. Surface energies were calculated based upon slabs with a minimum thickness of 20 Å, with surface energy converged against slab thickness. Full geometrical relaxation of the ionic positions was performed to incorporate surface relaxation effects.

ASSOCIATED CONTENT

Supporting Information

The Supporting Information is available free of charge on the ACS Publications website at DOI: 10.1021/acsnano.5b05535.

Additional experimental data (PDF)

Movie S1 (AVI)

AUTHOR INFORMATION

Corresponding Authors

*E-mail: rsyassar@uic.edu.

*E-mail: M.S.Islam@bath.ac.uk.

*E-mail: anie@mtu.edu.

*E-mail: junlu@anl.gov.

Notes

The authors declare no competing financial interest.

ACKNOWLEDGMENTS

R. Shahbazian-Yassar acknowledges financial support from the National Science Foundation (Award No. DMR-1410560). A. Nie and W. Yao were partially funded by NSF Award No. CMMI-1200383. Partial funding for Y. Yuan from Argonne National Laboratory under subcontract No. 4F31422 is acknowledged. J. Lu was supported by the U.S. Department of Energy under Contract DE-AC0206CH11357 from the Vehicle Technologies Office, Department of Energy, Office of Energy Efficiency and Renewable Energy (EERE). The acquisition of the UIC JEOL JEM-ARM200CF was supported by an MRI-R2 grant from the National Science Foundation (Award No. DMR-0959470). M. Islam acknowledges support from the EPSRC-funded CDT in Sustainable Chemical Technologies (EP/L016354) and Materials Chemistry consortium (EP/L000202/1) for Archer HPC/Archer facilities. This work made use of the JEOL JEM-ARM200CF in the Electron Microscopy Service (Research Resources Center, UIC). The acquisition of the UIC JEOL JEM-ARM200CF was supported by a MRI-R2 grant from the National Science Foundation [DMR-0959470]. We thank A. Nicholls and K. Low from RRC of UIC for the assistance on TEM sample preparation, E. Laitila from the Department of Materials Science and Engineering at MTU for his help with XRD experiments, and C. Fisher from JFCC, Nagoya, Japan, for helpful discussions.

REFERENCES

(1) Bursill, L. A.; Lodge, E. A.; Thomas, J. M. Zeolitic Structures as Revealed by High-Resolution Electron Microscopy. *Nature* **1980**, *286*, 111–113.

(2) Tao, Y.; Kanoh, H.; Abrams, L.; Kaneko, K. Mesopore-Modified Zeolites: Preparation, Characterization, and Applications. *Chem. Rev.* **2006**, *106*, 896–910.

(3) Behrens, E. A.; Clearfield, A. Titanium Silicates, $M_3HTi_4O_4(SiO_4)_3{\cdot}4H_2O$ (M = Na^+, K^+), with Three-Dimensional Tunnel Structures for the Selective Removal of Strontium and Cesium from Wastewater Solutions. *Microporous Mater.* **1997**, *11*, 65–75.

DOI: 10.1021/acsnano.5b05535
ACS Nano 2016, 10, 539–548

(4) Kijima, N.; Sakao, M.; Tanuma, Y.; Kataoka, K.; Igarashi, K.; Akimoto, J. Synthesis, Crystal Structure, and Electrochemical Properties of Hollandite-Type $K_xTi_{1-y}Mn_yO_2$. *Solid State Ionics* **2014**, *262*, 14−17.
(5) Zhang, H.; Banfield, J. F. Structural Characteristics and Mechanical and Thermodynamic Properties of Nanocrystalline TiO_2. *Chem. Rev.* **2014**, *114*, 9613−9644.
(6) Yuan, J.; Li, W.; Gomez, S.; Suib, S. L. Shape-Controlled Synthesis of Manganese Oxide Octahedral Molecular Sieve Three-Dimensional Nanostructures. *J. Am. Chem. Soc.* **2005**, *127*, 14184−14185.
(7) Chalmin, E.; Vignaud, C.; Menu, M. Palaeolithic Painting Matter: Natural or Heat-Treated Pigment? *Appl. Phys. A: Mater. Sci. Process.* **2004**, *79*, 187−191.
(8) Zhang, K.; Han, X.; Hu, Z.; Zhang, X.; Tao, Z.; Chen, J. Nanostructured Mn-Based Oxides for Electrochemical Energy Storage and Conversion. *Chem. Soc. Rev.* **2015**, *44*, 699−728.
(9) Chen, K.; Noh, Y. D.; Li, K.; Komarneni, S.; Xue, D. Microwave−Hydrothermal Crystallization of Polymorphic MnO_2 for Electrochemical Energy Storage. *J. Phys. Chem. C* **2013**, *117*, 10770−10779.
(10) Suib, S. L. Structure, Porosity, and Redox in Porous Manganese Oxide Octahedral Layer and Molecular Sieve Materials. *J. Mater. Chem.* **2008**, *18*, 1623−1631.
(11) Luo, J.; Zhang, Q.; Garcia-Martinez, J.; Suib, S. L. Adsorptive and Acidic Properties, Reversible Lattice Oxygen Evolution, and Catalytic Mechanism of Cryptomelane-Type Manganese Oxides as Oxidation Catalysts. *J. Am. Chem. Soc.* **2008**, *130*, 3198−3207.
(12) Cao, Y.; Xiao, L.; Wang, W.; Choi, D.; Nie, Z.; Yu, J.; Saraf, L. V.; Yang, Z.; Liu, J. Reversible Sodium Ion Insertion in Single Crystalline Manganese Oxide Nanowires with Long Cycle Life. *Adv. Mater.* **2011**, *23*, 3155−3160.
(13) Simon, P.; Gogotsi, Y. Materials for Electrochemical Capacitors. *Nat. Mater.* **2008**, *7*, 845−854.
(14) Cai, J.; Liu, J.; Gao, Z.; Navrotsky, A.; Suib, S. L. Synthesis and Anion Exchange of Tunnel Structure Akaganeite. *Chem. Mater.* **2001**, *13*, 4595−4602.
(15) Sui, N.; Duan, Y.; Jiao, X.; Chen, D. Large-Scale Preparation and Catalytic Properties of One-Dimensional α/β-MnO_2 Nanostructures. *J. Phys. Chem. C* **2009**, *113*, 8560−8565.
(16) Devaraj, S.; Munichandraiah, N. Effect of Crystallographic Structure of MnO_2 on Its Electrochemical Capacitance Properties. *J. Phys. Chem. C* **2008**, *112*, 4406−4417.
(17) Wang, H.; Lu, Z.; Qian, D.; Li, Y.; Zhang, W. Single-Crystal α-MnO_2 Nanorods: Synthesis and Electrochemical Properties. *Nanotechnology* **2007**, *18*, 115616−115620.
(18) Zhang, X.; Yang, W.; Yang, J.; Evans, D. G. Synthesis and Characterization of α-MnO_2 Nanowires: Self-Assembly and Phase Transformation to β-MnO_2 Microcrystals. *J. Cryst. Growth* **2008**, *310*, 716−722.
(19) Portehault, D.; Cassaignon, S.; Baudrin, E.; Jolivet, J. P. Morphology Control of Cryptomelane Type MnO_2 Nanowires by Soft Chemistry. Growth Mechanisms in Aqueous Medium. *Chem. Mater.* **2007**, *19*, 5410−5417.
(20) Khan, M.; Yohannes, E.; Powell, D. Synthesis and Characterization of a New Mixed-Metal Oxide Framework Material Composed of Vanadium Oxide Clusters: X-Ray Crystal Structure of $(N_2H_5)_2[Zn_3V^{IV}{}_{12}V^{V}{}_6O_{42}(SO_4)(H_2O)_{12}]\cdot 24H_2$. *Chem. Commun.* **1999**, *1*, 23−24.
(21) Xu, M.; Kong, L.; Zhou, W.; Li, H. Hydrothermal Synthesis and Pseudocapacitance Properties of α-MnO_2 Hollow Spheres and Hollow Urchins. *J. Phys. Chem. C* **2007**, *111*, 19141−19147.
(22) Santhanagopalan, S.; Balram, A.; Meng, D. D. Scalable High-Power Redox Capacitors with Aligned Nanoforests of Crystalline MnO_2 Nanorods by High Voltage Electrophoretic Deposition. *ACS Nano* **2013**, *7*, 2114−2125.
(23) Wang, X.; Li, Y. Selected-Control Hydrothermal Synthesis of α- and β-MnO_2 Single Crystal Nanowires. *J. Am. Chem. Soc.* **2002**, *124*, 2880−2881.
(24) Li, W.; Yuan, J.; Shen, X.; Gomez-Mower, S.; Xu, L.; Sithambaram, S.; Aindow, M.; Suib, S. L. Hydrothermal Synthesis of Structure- and Shape-Controlled Manganese Oxide Octahedral Molecular Sieve Nanomaterials. *Adv. Funct. Mater.* **2006**, *16*, 1247−1253.
(25) Galindo, H. M.; Carvajal, Y.; Njagi, E.; Ristau, R. A.; Suib, S. L. Facile One-Step Template-Free Synthesis of Uniform Hollow Microstructures of Cryptomelane-Type Manganese Oxide K-OMS-2. *Langmuir* **2010**, *26*, 13677−13683.
(26) Lan, B.; Yu, L.; Lin, T.; Cheng, G.; Sun, M.; Ye, F.; Sun, Q.; He, J. Multifunctional Free-Standing Membrane from the Self-Assembly of Ultralong MnO_2 Nanowires. *ACS Appl. Mater. Interfaces* **2013**, *5*, 7458−7464.
(27) Li, D.; Nielsen, M. H.; Lee, J. R. I.; Frandsen, C.; Banfield, J. F.; Yoreo, J. J. D. Direction-Specific Interactions Control Crystal Growth by Oriented Attachment. *Science* **2012**, *336*, 1014−1018.
(28) Zhang, Q.; Liu, S. J.; Yu, S. H. Recent Advances in Oriented Attachment Growth and Synthesis of Functional Materials: Concept, Evidence, Mechanism, and Future. *J. Mater. Chem.* **2009**, *19*, 191−207.
(29) Cho, K. S.; Talapin, D. V.; Gaschler, W.; Murray, C. B. Designing PbSe Nanowires and Nanorings through Oriented Attachment of Nanoparticles. *J. Am. Chem. Soc.* **2005**, *127*, 7140−7147.
(30) Banfield, J. F.; Welch, S. A.; Zhang, H.; Ebert, T. T.; Penn, R. L. Aggregation-Based Crystal Growth and Microstructure Development in Natural Iron Oxyhydroxide Biomineralization Products. *Science* **2000**, *289*, 751−754.
(31) Pacholski, C.; Kornowski, A.; Weller, H. Self-Assembly of ZnO: From Nanodots to Nanorods. *Angew. Chem., Int. Ed.* **2002**, *41*, 1188−1191.
(32) Turner, S.; Buseck, P. R. Defects in Nsutite (γ-MnO_2) and Dry-Cell Efficiency. *Nature* **1983**, *304*, 143−146.
(33) Turner, S.; Buseck, P. R. Manganese Oxide Tunnel Structures and Their Intergrowths. *Science* **1979**, *203*, 456−458.
(34) Shen, X.; Ding, Y.; Liu, J.; Cai, J.; Laubernds, K.; Zerger, R. P.; Vasiliev, A.; Aindow, M.; Suib, S. L. Control of Nanometer-Scale Tunnel Sizes of Porous Manganese Oxide Octahedral Molecular Sieve Nanomaterials. *Adv. Mater.* **2005**, *17*, 805−809.
(35) Leclaire, A.; Borel, M. M.; Grandin, A.; Raveau, B. Two Molybdenum Diphosphates with a Tunnel Structure Involving Mo(III): $KMoP_2O_7$ and $K_{0.17}MoP_2O_7$. *J. Solid State Chem.* **1989**, *78*, 220−226.
(36) Williamson, M. J.; Tromp, R. M.; Vereecken, P. M.; Hull, R.; Ross, F. M. Dynamic Microscopy of Nanoscale Cluster Growth at the Solid−Liquid Interface. *Nat. Mater.* **2003**, *2*, 532−536.
(37) Zheng, H.; Smith, R. K.; Jun, Y.; Kisielowski, C.; Dahmen, U.; Alivisatos, A. P. Observation of Single Colloidal Platinum Nanocrystal Growth Trajectories. *Science* **2009**, *324*, 1309−1312.
(38) Smeets, P. J. M.; Cho, K. R.; Kempen, R. G. E.; Sommerdijk, N. A. J. M.; Yoreo, J. J. D. Calcium Carbonate Nucleation Driven by Ion Binding in a Biomimetic Matrix Revealed by *in situ* Electron Microscopy. *Nat. Mater.* **2015**, *14*, 394−399.
(39) Grogan, J. M.; Schneider, N. M.; Ross, F. M.; Bau, H. H. Bubble and Pattern Formation in Liquid Induced by an Electron Beam. *Nano Lett.* **2014**, *14*, 359−364.
(40) Schneider, N. M.; Norton, M. M.; Mendel, B. J.; Grogan, J. M.; Ross, F. M.; Bau, H. H. Electron−Water Interactions and Implications for Liquid Cell Electron Microscopy. *J. Phys. Chem. C* **2014**, *118*, 22373−22382.
(41) Liu, J.; Makwana, V.; Cai, J.; Suib, S. L.; Aindow, M. Effects of Alkali Metal and Ammonium Cation Templates on Nanofibrous Cryptomelane-Type Manganese Oxide Octahedral Molecular Sieves (OMS-2). *J. Phys. Chem. B* **2003**, *107*, 9185−9194.
(42) Penn, R. L.; Banfield, J. F. Imperfect Oriented Attachment: Dislocation Generation in Defect-Free Nanocrystals. *Science* **1998**, *281*, 969−971.
(43) Shen, X.; Ding, Y.; Liu, J.; Laubernds, K.; Zerger, R. P.; Polverejan, M.; Son, Y. C.; Aindow, M.; Suib, S. L. Synthesis, Characterization, and Catalytic Applications of Manganese Oxide

DOI: 10.1021/acsnano.5b05535
ACS Nano 2016, 10, 539−548

Octahedral Molecular Sieve (OMS) Nanowires with a 2 × 3 Tunnel Structure. *Chem. Mater.* **2004**, *16*, 5327−5335.
(44) Tompsett, D. A.; Parker, S. C.; Islam, M. S. Surface Properties of α-MnO_2: Relevance to Catalytic and Supercapacitor Behaviour. *J. Mater. Chem. A* **2014**, *2*, 15509−15518.
(45) Tompsett, D. A.; Islam, M. S. Electrochemistry of Hollandite α-MnO_2: Li-Ion and Na-Ion Insertion and Li_2O Incorporation. *Chem. Mater.* **2013**, *25*, 2515−2526.
(46) Islam, M. S.; Fisher, C. A. Lithium and Sodium Battery Cathode Materials: Computational Insights into Voltage, Diffusion and Nanostructural Properties. *Chem. Soc. Rev.* **2014**, *43*, 185−204.
(47) Arthur, T. S.; Zhang, R.; Ling, C.; Glans, P. A.; Fan, X.; Guo, J.; Mizuno, F. Understanding the Electrochemical Mechanism of K-αMnO_2 for Magnesium Battery Cathodes. *ACS Appl. Mater. Interfaces* **2014**, *6*, 7004−7008.
(48) Li, W.; Cui, X.; Zeng, R.; Du, G.; Sun, Z.; Zheng, R.; Ringer, S. P.; Dou, S. Performance Modulation of α-MnO_2 Nanowires by Crystal Facet Engineering. *Sci. Rep.* **2015**, *5*, 8987.
(49) Li, L.; Nan, C.; Lu, J.; Peng, Q.; Li, Y. α-MnO_2 Nanotubes: High Surface Area and Enhanced Lithium Battery Properties. *Chem. Commun.* **2012**, *48*, 6945−6947.
(50) Yuan, Y.; Nie, A.; Odegard, G. M.; Xu, R.; Zhou, D.; Santhanagopalan, S.; He, K.; Asayesh-Ardakani, H.; Meng, D. D.; Klie, R. F.; et al. Asynchronous Crystal Cell Expansion during Lithiation of K^+-Stabilized α-MnO_2. *Nano Lett.* **2015**, *15*, 2998−3007.
(51) Yang, P.; Ding, Y.; Lin, Z.; Chen, Z.; Li, Y.; Qiang, P.; Ebrahimi, M.; Mai, W.; Wong, C. P.; Wang, Z. L. Low-Cost High-Performance Solid-State Asymmetric Supercapacitors Based on MnO_2 Nanowires and Fe_2O_3 Nanotubes. *Nano Lett.* **2014**, *14*, 731−736.
(52) Zhai, D.; Li, B.; Xu, C.; Du, H.; He, Y.; Wei, C.; Kang, F. A Study on Charge Storage Mechanism of α-MnO_2 by Occupying Tunnels with Metal Cations (Ba^{2+}, K^+). *J. Power Sources* **2011**, *196*, 7860−7867.
(53) Xiao, W.; Xia, H.; Fuh, J. Y. H.; Lu, J. Growth of Single-Crystal α-MnO_2 Nanotubes Prepared by a Hydrothermal Route and Their Electrochemical Properties. *J. Power Sources* **2009**, *193*, 935−938.
(54) Qin, Y.; Lu, J.; Du, P.; Chen, Z.; Ren, Y.; Wu, T.; Miller, J. T.; Wen, J.; Miller, D. J.; Zhang, Z.; et al. *In Situ* Fabrication of Porous-Carbon-Supported α-MnO_2 Nanorods at Room Temperature: Application for Rechargeable Li-O_2 Batteries. *Energy Environ. Sci.* **2013**, *6*, 519−531.
(55) Hutchings, G. S.; Rosen, J.; Smiley, D.; Goward, G. R.; Bruce, P. G.; Jiao, F. Environmental *In Situ* X-Ray Absorption Spectroscopy Evaluation of Electrode Materials for Rechargeable Lithium-Oxygen Batteries. *J. Phys. Chem. C* **2014**, *118*, 12617−12624.
(56) Truong, T. T.; Liu, Y.; Ren, Y.; Trahey, L.; Sun, Y. Morphological and Crystalline Evolution of Nanostructured MnO_2 and Its Application in Lithium−Air Batteries. *ACS Nano* **2012**, *6*, 8067−8077.
(57) Débart, A.; Paterson, A. J.; Bao, J.; Bruce, P. G. α-MnO_2 Nanowires: A Catalyst for the O_2 Electrode in Rechargeable Lithium Batteries. *Angew. Chem.* **2008**, *120*, 4597−4600.
(58) Du, N.; Zhang, H.; Chen, B.; Ma, X.; Yang, D. Ligand-Free Self-Assembly of Ceria Nanocrystals into Nanorods by Oriented Attachment at Low Temperature. *J. Phys. Chem. C* **2007**, *111*, 12677−12680.
(59) Wang, X.; Li, Y. Synthesis and Formation Mechanism of Manganese Dioxide Nanowires/Nanorods. *Chem. - Eur. J.* **2003**, *9*, 300−306.
(60) Portehault, D.; Cassaignon, S.; Baudrinc, E.; Jolivet, J. P. Structural and Morphological Control of Manganese Oxide Nanoparticles upon Soft Aqueous Precipitation through MnO_4^-/Mn^{2+} Reaction. *J. Mater. Chem.* **2009**, *19*, 2407−2416.
(61) Ding, Y.; Shen, X.; Sithambaram, S.; Gomez, S.; Kumar, R.; Crisostomo, V. M. B.; Suib, S. L.; Aindow, M. Synthesis and Catalytic Activity of Cryptomelane-Type Manganese Dioxide Nanomaterials Produced by a Novel Solvent-Free Method. *Chem. Mater.* **2005**, *17*, 5382−5389.
(62) Kresse, G.; Furthmuller, J. Efficient Iterative Schemes for *ab initio* Total-Energy Calculations using a Plane-Wave Basis Set. *Phys. Rev. B: Condens. Matter Mater. Phys.* **1996**, *54*, 11169−11186.
(63) Perdew, J. P.; Burke, K. Generalized Gradient Approximation Made Simple. *Phys. Rev. Lett.* **1996**, *77*, 3865−3868.
(64) Armstrong, A. R.; Lyness, C.; Panchmatia, P. M.; Islam, M. S.; Bruce, P. G. The Lithium Intercalation Process in the Low Voltage Lithium Battery Anode $Li_{1+x}V_{1-x}O_2$. *Nat. Mater.* **2011**, *10*, 223−229.

DOI: 10.1021/acsnano.5b05535
ACS Nano 2016, 10, 539−548